MICROMECHANICAL MODELING OF MIXED-MODE CRACK GROWTH IN CERAMIC COMPOSITES

J. Zhai and M. Zhou

J. Zhai[1] *and M. Zhou*[1]

Micromechanical Modeling of Mixed-Mode Crack Growth in Ceramic Composites

REFERENCE: Zhai, J. and Zhou, M., **"Micromechanical Modeling of Mixed-Mode Crack Growth in Ceramic Composites,"** *Mixed-Mode Crack Behavior, ASTM STP 1359,* K. J. Miller and D. L. McDowell, Eds., American Society for Testing and Materials, West Conshohocken, PA, 1999, pp. 174–200.

ABSTRACT: Dynamic crack propagation in ceramic composites is analyzed numerically. The simulations concern the effects of microstructural morphologies on fracture. The analysis considers arbitrary phase distributions in the actual microstructures of alumina/titanium diboride (Al_2O_3/TiB_2) composites. The microstructures analyzed have different phase morphologies and different phase sizes over an order of magnitude in length (from 1–2 to 10–20 μm). A micromechanical model that provides explicit account for arbitrary microstructures and arbitrary fracture patterns is developed and used. The approach uses both a constitutive law for the bulk solid constituents and a constitutive law for fracture surfaces. The model is based on the cohesive surface formulation of Xu and Needleman and represents a phenomenological characterization for atomic forces on potential crack/microcrack surfaces. This framework of analysis does not require the use of any fracture criteria. Instead, fracture evolves as an outcome of bulk material response, interfacial behavior, and applied loading. This approach provides a unified and self-consistent treatment of mixed mode fracture. The evolutions of crack lengths in different phases and along interphase interfaces are calculated to track crack growth. The overall local crack speed, defined as the time rate of change of arc length along zigzagging crack paths, is found to reach the intersonic range, i.e., greater than the shear wave speeds and smaller than the longitudinal wave speeds in the constituent phases. The model also allows the energy release rate to be evaluated easily. For the same amount of crack surfaces generated, the average energy release rates for fracture patterns in four microstructures analyzed differ by up to 25%. The results demonstrate that larger TiB_2 reinforcements significantly impede crack propagation and increase the fracture resistance of the composites, as indicated by higher average energy release rate values.

KEYWORDS: micromechanical modeling, cohesive force, fracture, inhomogeneous materials, elasticity, mixed-mode fracture, fracture mode, numerical simulation, crack propagation, ceramic composites

Nomenclature

C_L	Longitudinal wave velocity
C_s	Shear wave velocity
C_R	Rayleigh wave velocity
τ_{max}	Maximum shear stress for a cohesive surface pair
σ_{max}	Maximum tensile stress for a cohesive surface pair
δ_n	Characteristic length for normal separation
δ_t	Characteristic length for tangential separation

[1] The George W. Woodruff School of Mechanical Engineering, Georgia Institute of Technology, Atlanta, GA 30332-0405. (M. Zhou is author to whom correspondence should be addressed.)

ϕ_0 Surface energy per unit area
ϕ_{crack} Fracture energy associated with crack growth
$\partial\phi_{crack}/\partial a$ Energy release rate per apparent crack growth
$\partial\phi_{crack}/\partial l$ Energy release rate per local crack growth

Microscopically inhomogeneous materials derive significantly higher strength and toughness from microscopic reinforcements such as fibers and particles. The enhancement is due to the higher toughness and strength of the additional phases and deformation mechanisms that do not come into play for monolithic materials. In addition to different length scales associated with material inhomogeneities, different time scales are also introduced by composite microstructures under transient loading due to different stress wave speeds or the inertia effect. These spatial and temporal effects provide opportunities for material property enhancement through multiple deformation and failure mechanisms. For example, material inhomogeneities and reinforcements force cracks to follow tortuous paths therefore increasing dissipation and fracture resistance. Micromechanical modeling and simulation represents a unique and attractive means for delineating the effects of micro and meso failure mechanisms. The dynamic failure of brittle materials has been extensively analyzed, for example, [*1–20*]. Most available models for the failure are, for the most part, continuum damage theories in which the net effect of fracture is idealized as a degradation of the elasticity modulus, for example, see Refs *21–29*. While capturing the macroscopic or effective response, these models do not explicitly consider the discrete nature of fracture through crack growth and coalescence. Thus, the models lack the ability to account for the interaction between cracks and resolve specific failure modes and failure patterns. In addition, the effects of microstuctural inhomogeneities of different size scales such as inclusions, fibers, and grains on crack path and fracture toughness cannot be explicitly analyzed.

The complex morphologies of material microstructures precludes the application of analytical methods. Explicit micromechanical modeling and simulation represent a unique means for analyzing micro and meso failure and for elucidating scaling laws. Through the consideration of representative samples of actual microstructures, the effects of various fracture mechanisms can be delineated. The required features of this framework should: (1) allow explicit account of real, arbitrary material microstructures, (2) permit explicit modeling of fracture in a nonconstrained (arbitrary crack paths or microcrack patterns) manner, and (3) be free of limitations of fracture criteria applicable only over certain length scales (such as continuum criteria that assume the existence of *K*-fields). Combined use of the cohesive surface approach of Xu and Needleman [*30,31*] and bulk constitutive laws is a good candidate for providing such a framework. Explicit simulation of fracture and fragmentation have also been carried out by Camacho and Ortiz [*32*] and Ortiz [*33*] using a cohesive model in the analysis of dynamic failure of materials.

Alumina/titanium diboride (Al_2O_3/TiB_2) composites with a wide range of microstructural morphologies demonstrate a range of failure resistance and a strong dependence of fracture toughness on microstructure in experiments, see Logan [*34*]. These materials are composed of titanium diboride (TiB_2) reinforcements embedded in a matrix of alumina (Al_2O_3). The principal modes of failure observed in experiments are transgranular and intergranular fracture of Al_2O_3 matrix, reflecting the effects of different phase distributions, different size scales, and different interfacial bonding strengths that result from various processing conditions. For example, the principal mode of failure is interfacial fracture through microcrack formation when a weak interfacial bonding between the constituents is found. Clearly, interfacial strength significantly influences the overall behavior of the composites. A numerical analysis on the effect of interfacial strength on failure modes has been conducted in Zhai

and Zhou [*35*]. The analyses here concern the effects of microstructure on the fracture resistance of Al_2O_3/TiB_2 composites. The focus is crack path, crack speed, and energy release rate. Explicit account is taken of arbitrary crack and microcrack fracture patterns as well as of arbitrary microstructures. As in Xu et al. [*30*], the crack surfaces are regarded as cohesive surfaces exhibiting traction forces that are functions of interfacial separations. These relations represent phenomenological characterizations of the atomistic attraction and repulsion forces that vary with inter-atomic displacements. All finite element boundaries between elements are cohesive surfaces serving as potential crack paths. Arbitrary crack and microcrack patterns can be resolved through the use of fine meshes. This approach does not require any crack initiation and propagation criterion. Instead, the cohesive surface constitutive law allows fracture to evolve as a natural outcome of the combined effects of bulk constituent response, interfacial behavior, and applied loading.

Problem Formulation

To account for the finite strains involved in crack tip regions, a Lagrangian finite deformation formulation is used. The independent variables are the position of a material point in the reference configuration $\boldsymbol{x}$, and time t. Relative to a fixed Cartesian frame $\{\xi^i\}$, a material point initially at $\boldsymbol{x}$ occupies position $\bar{\boldsymbol{x}}$ in the current configuration. The displacement vector and the deformation gradient are defined as $\boldsymbol{u} = \bar{\boldsymbol{x}} - \boldsymbol{x}$ and $\boldsymbol{F} = \partial\bar{\boldsymbol{x}}/\partial\boldsymbol{x}$, respectively. The principle of virtual work includes a contribution from the cohesive surfaces and is written as

$$\int_V \boldsymbol{s}:\delta\boldsymbol{F}dV - \int_{S_{\text{int}}} \boldsymbol{T}\cdot\delta\boldsymbol{\Delta}dS = \int_{S_{\text{ext}}} \boldsymbol{T}\cdot\delta\boldsymbol{u}dS - \int_V \rho\frac{\partial^2\boldsymbol{u}}{\partial t^2}\cdot\delta\boldsymbol{u}dV \tag{1}$$

where $\boldsymbol{s}$: $\delta\boldsymbol{F} = s^{ij}\delta F_{ji}$, $\boldsymbol{s}$ is the nonsymmetric first Piola-Kirchhoff stress; $\boldsymbol{\Delta}$ is the displacement jump across a pair of cohesive surfaces; V, S_{ext} and S_{int} are the volume, external surface area, and internal cohesive surface area, respectively, of the body in the reference configuration. The density of the material in the reference configuration is ρ. Also, $\delta\boldsymbol{F}$, $\delta\boldsymbol{\Delta}$ and $\delta\boldsymbol{u}$ denote admissible variations $\boldsymbol{F}$, $\boldsymbol{\Delta}$ and $\boldsymbol{u}$ respectively. The traction vector $\boldsymbol{T}$ and the surface normal in the reference configuration $\boldsymbol{n}$ are related through $\boldsymbol{T} = \boldsymbol{n}\cdot\boldsymbol{s}$. The volumetric constitutive law is hyperelastic so that

$$\boldsymbol{S} = \frac{\partial W}{\partial \boldsymbol{E}} \tag{2}$$

where $\boldsymbol{S} = \boldsymbol{s}\cdot\boldsymbol{F}^{-T}$ is the second Piola-Kirchhoff stress. The strain energy density W is taken to be

$$W = \frac{1}{2}\boldsymbol{E}:\boldsymbol{L}:\boldsymbol{E} \tag{3}$$

with

$$\boldsymbol{L} = \frac{E}{1+\upsilon}\left(\boldsymbol{II} + \frac{\upsilon}{1-2\upsilon}\boldsymbol{I}\otimes\boldsymbol{I}\right) \tag{4}$$

being the tensor of isotropic elastic moduli. $\boldsymbol{E}$ and v are the Young's modulus and Poisson's ratio, respectively. $\boldsymbol{E}$ is the Lagrangian strain given by

$$\boldsymbol{E} = \frac{1}{2}(\boldsymbol{F}^T \cdot \boldsymbol{F} - \boldsymbol{I}) \tag{5}$$

Also in the above formulas, $\boldsymbol{II}$ is the fourth order identity tensor, $\boldsymbol{I}$ is the second order identity tensor, $\boldsymbol{I}\otimes\boldsymbol{I}$ denotes the tensor product of two second order tensors, and $(\ )^T$ and $(\ )^{-T}$ denote inverse and inverse transpose, respectively.

The constitutive law for cohesive surfaces relates the traction and displacement jumps across crack surfaces and is also taken to be hyperelastic so that any dissipation associated with separation is neglected. Assuming the surface potential energy is ϕ, the traction on the cohesive surfaces can be derived through

$$\boldsymbol{T} = \frac{\partial \phi}{\partial \boldsymbol{\Delta}} \tag{6}$$

In two dimensions, the specific form of ϕ used here is

$$\phi(\Delta) = \phi_0 - \phi_0\left(1 + \frac{\Delta_n}{\delta_n}\right)\exp\left(-\frac{\Delta_n}{\delta_n}\right)\exp\left(-\frac{\Delta_t^2}{\delta_t^2}\right) \tag{7}$$

where $\Delta_n = \boldsymbol{n} \cdot \boldsymbol{\Delta}$ and $\Delta_t = \boldsymbol{t} \cdot \boldsymbol{\Delta}$ are the normal and tangential displacement jumps, with $\boldsymbol{n}$ and $\boldsymbol{t}$ denoting unit vectors along the surface normal and tangent in the reference configuration, respectively. Potential ϕ is written such that $\phi(\Delta)|_{|\Delta|=0} = 0$ and therefore $\phi_0 = \phi(\boldsymbol{\Delta})|_{|\Delta|\to\infty}$ is the work of separation. Two special paths of decohesion are considered to illustrate the variations of the cohesive traction components. The first path is pure normal separation with tangential traction component $T_t = \boldsymbol{t} \cdot \boldsymbol{T} = 0$ and tangential separation $\Delta_t = 0$. The second path is pure tangential separation with normal traction component $T_n = \boldsymbol{t} \cdot \boldsymbol{T} = 0$ and normal separation $\Delta_n = 0$. The works of normal and tangential separations along these two paths are equal to each other and are taken to be $\phi_0 = e\sigma_{\max}\,\delta_n = \sqrt{e/2}\tau_{\max}\,\delta_t$, with $e = \exp(1) = 2.718281829$. δ_n and $\delta_t/\sqrt{2}$ are normal and shear displacement jump values at which maximum normal stress $\sigma_{\max}$ and maximum shear stress $\tau_{\max}$ occur, respectively.

The cohesive surface taction components obtained from Eqs 6 and 7 are

$$T_n(\boldsymbol{\Delta}) = \frac{\phi_0\Delta_n}{\delta_n^2}\exp\left(-\frac{\Delta_n}{\delta_n}\right)\exp\left(-\frac{\Delta_t^2}{\delta_t^2}\right) \tag{8}$$

and

$$T_t(\boldsymbol{\Delta}) = -\frac{2\phi_0\Delta_t}{\delta_t^2}\left(1 + \frac{\Delta_n}{\delta_n}\right)\exp\left(-\frac{\Delta_n}{\delta_n}\right)\exp\left(-\frac{\Delta_t^2}{\delta_t^2}\right) \tag{9}$$

These relations are illustrated in Fig. 1. Clearly, there are cross dependencies of normal traction on shear displacement jumps and shear traction on normal displacement jumps. When displacement jumps exceed certain values, both traction components decrease with further increase in separations and approach zero as $|\boldsymbol{\Delta}| \to \infty$. Under negative normal sepa-

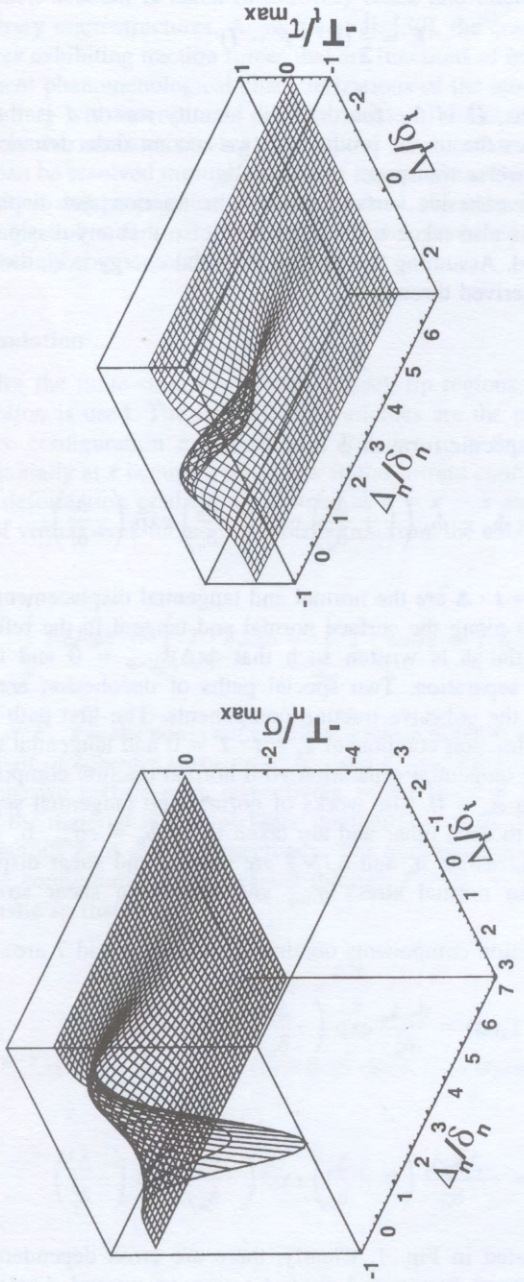

FIG. 1—*An illustration of the constitutive behavior of cohesive surfaces, (a) normal traction, (b) shear traction.*

rations (interpenetration), the normal traction component increases rapidly, simulating the strong atomistic repulsion during compression.

The balance of energy requires that the total external work $\mathcal{P}$ done to a body to be equal to the sum of the strain energy $\mathcal{W}$ stored in the bulk material, the kinetic energy $\mathcal{K}$ in the body and the cohesive surface energy Φ, meaning

$$\mathcal{P} = \int_{S_{\text{text}}} \boldsymbol{T} \cdot \boldsymbol{u} dS = \mathcal{K} + \mathcal{W} + \Phi \tag{10}$$

where

$$\left.\begin{aligned} \mathcal{K} &= \int_V \frac{1}{2} \rho \frac{\partial \boldsymbol{u}}{\partial t} \cdot \frac{\partial \boldsymbol{u}}{\partial t} dV \\ \mathcal{W} &= \int_V W dV \end{aligned}\right\} \tag{11}$$

and

$$\Phi = \int_{S_{\text{int}}} \phi dS$$

The cohesive energy Φ is the amount of energy spent on generating new crack surfaces, therefore represents a measure of the energy consumption on fracture. Under the same loading conditions, the higher the Φ required for generating the same amount of crack surfaces, the higher the fracture resistance of the material. In the analyses carried out there, this energy is used to compare the fracture resistance of specimens with different microstructures under the same overall remote loading.

Problem Analyzed

Computations are carried out for a center-cracked specimen, as illustrated in Fig. 2. The specimen has an initial height of $2H = 1.6$ mm and an initial width of $2L = 1.6$ mm. An initial crack of length $2a_i = 0.4$ mm exists along the ξ^1 axis. Only one half of the specimen ($\xi^1 > 0$) is discretized and modeled in the simulations because of symmetry with respect to the ξ^2 axis. Conditions of plain strain are assumed to prevail. The small region in front of the crack tip contains microstructures digitized from micrographs of actual composite materials, see Fig. 3. Inside this region, the material inhomogeneities and material phase distribution are explicitly modeled. The dimensions for this region are limited by the memory sizes of the Cray T90 and J90 computers used in this work. As seen below, the particular dimensions chosen here (100 by 200 μm) are much larger than most size scales in the microstructures analyzed. Digitized microstructures of actual Al_2O_3/TiB_2 composites shown in Fig. 4 are used in the analyses. In these micrographs, the Al_2O_3 matrix appears lighter and the harder TiB_2 reinforcements appear darker. These microstructures have TiB_2 volume fractions between 15 to 25%. In microstructures (*a–c*), the TiB_2 particles are embedded in the alumina matrix. The average grain size is approximately 10–20 μm for (*a*), 8–10 μm for (*b*), and 1–2 μm for (*c*). The composite microstructure in Fig. 4(*d*) consists of a population of isolated Al_2O_3 matrix islands surrounded by a network of TiB_2 reinforcements. The isolated matrix areas are approximately 20 by 100 μm in size. A dispersion of small Al_2O_3 particles several microns in size are scattered in the TiB_2 phase. Clearly, two length scales

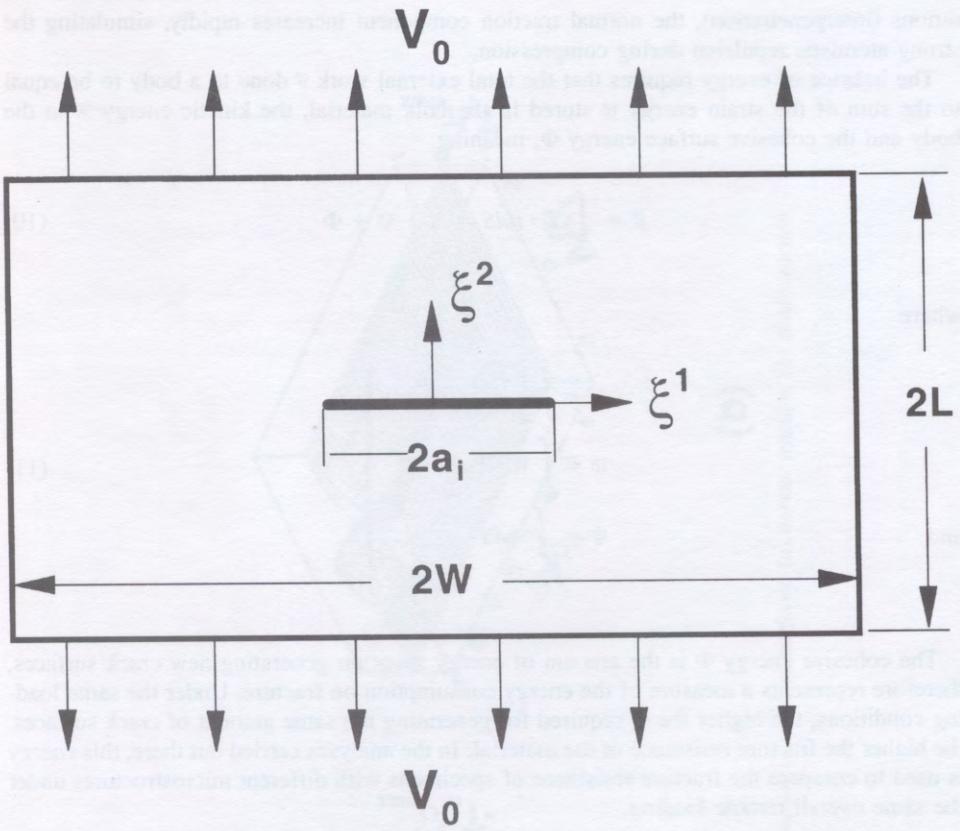

FIG. 2—*Problem analyzed: a centered-cracked specimen under tensile loading.*

are operative in this microstructure, influencing its deformation and failure, and consequently determining its strength and fracture toughness. The different microstructural phase morphologies are the result of different conditions during hot pressing, see Logan [*34*]. Partly because of the differences in their microstructures, these materials have shown a range of fracture toughness and failure resistance. The current analyses focus on the effects of these different phase morphologies on the fracture behavior of the specimen shown in Fig. 2. The effects of different interfacial bonding strengths that may also result from the different processing conditions are not specifically analyzed here. Some results concerning the influence of interphase bonding strength on failure modes in these materials are given in Zhai et al. [*35*]. In the current analyses, each of the phases behaves hyperelastically. Depending on material properties, boundary conditions, and loading, fracture is possible inside each of the phases and along the interfaces between the phases. The bulk properties of each finite element are those for either the grains or those for the matrix. The properties of each segment of potential fracture surface are specified according to location as those belonging to the matrix, the reinforcements or the matrix/reinforcement interfaces. The material and model parameters are listed in Table 1 (bulk properties) and Table 2 (cohesive surface constitutive properties). For comparison and analysis purposes, the speeds for the longitudinal stress waves (c_L), the shear stress waves (c_s) and the Rayleigh surface waves (c_R) are also listed in Table

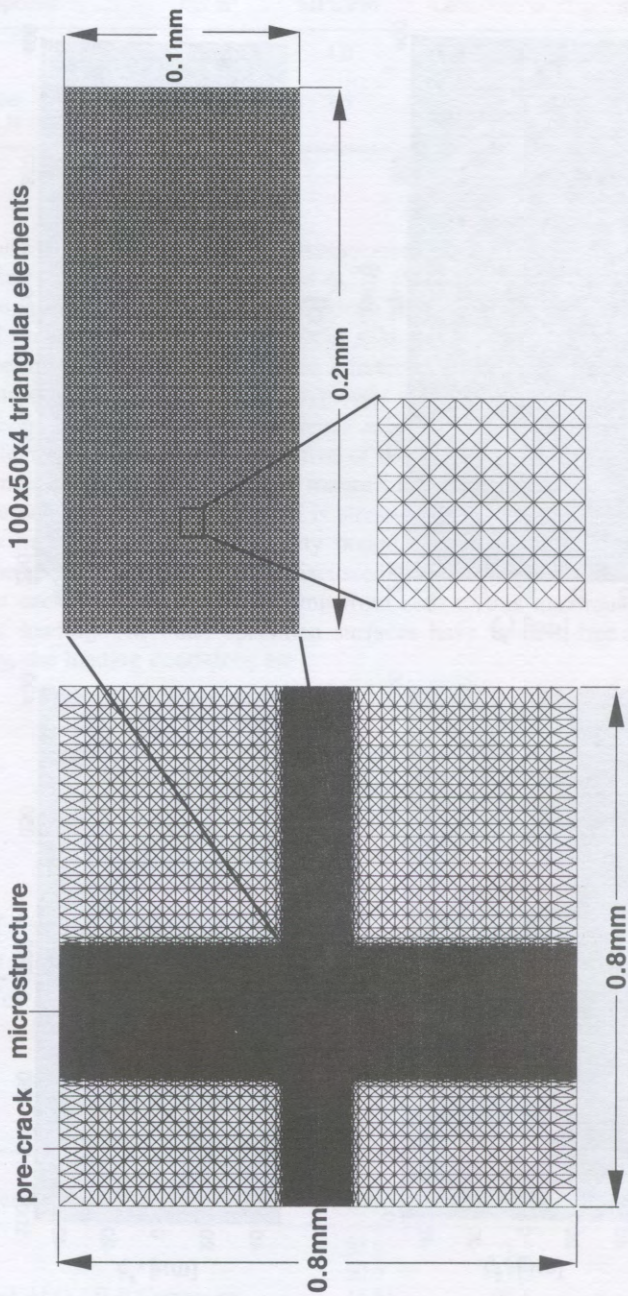

FIG. 3—*Finite element model and mesh for the specimen.*

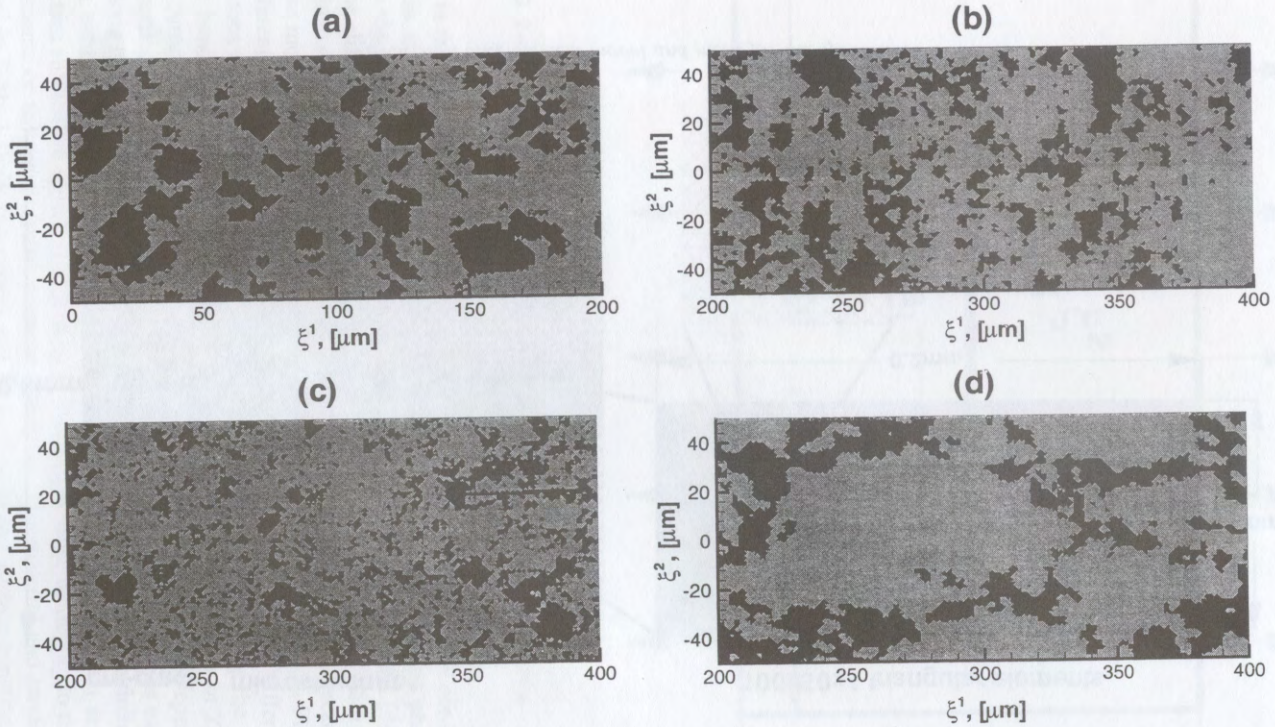

FIG. 4—*Microstructural morphologies analyzed;* (a) *TiB_2 embedded in Al_2O_3, grain size is 10–20 μm,* (b) *TiB_2 embedded in Al_2O_3, grain size is 8–10 μm,* (c) *TiB_2 embedded in Al_2O_3, grain size is 1–2 μm,* (d) *a network of TiB_2 filled with Al_2O_3, cell size is approximately 100 μm.*

TABLE 1—*Bulk material properties.*

Compound	Density kg/m^3	K_{IC}, MPa$\sqrt{\text{m}}$	E, GPa	υ	c_L, m/s	c_s, m/s	c_R, m/s
Al_2O_3	3990	4.0	340	0.23	9 939	5885	5379
TiB_2	4520	7.2	500	0.12	10 694	7027	6267
Homogenized Al_2O_3/Ti_2B Composite	4120	3.6	415	0.15	10 300	6609	5936

1. The choice of the cohesive law parameters assumes that $\sigma_{max} = E/10$ for each constituent with E being the Young's modulus and $\phi_0 = (1 - \upsilon^2)K_{IC}^2/E$ with K_{IC} being the Mode I fracture toughness of the materials in question. The parameters for the Al_2O_3/TiB_2 interfaces are chosen such that the maximum stress σ_{max} is lower than that for either the matrix or the reinforcements. Specifically, both σ_{max} of interfacial work of separation ϕ_0 are 1–3 of those for the matrix, consistent with what is typically reported for ceramic composites.

Materials outside the crack-tip region are assumed to be homogeneous and are assigned a set of effective parameters representative of those for the Al_2O_3/TiB_2 ceramic composite. Both regions are discretized in the same manner, using both the bulk and the cohesive surface constitutive descriptions. The specimen is stress-free and at rest initially. Tensile loading is applied by imposing symmetric velocity boundary conditions along the upper and lower edges of the specimen. For the results discussed here, the imposed boundary velocity is $V_0 =$ 10 m/s for each edge with a linear ramp from zero to this maximum velocity in the first 0.01 μs of loading. All other specimen surfaces have traction-free boundary conditions. Specifically, the loading conditions are

$$u^2(\xi^1, \pm H, t) = \begin{cases} \pm \dfrac{t}{0.001} V_0, & t < 0.01\ \mu s \\ \pm V_0 & t > 0.001\ \mu s \end{cases} \quad -L < \xi^1 < L \tag{12}$$

$$T^1(\xi^1, \pm H, t) = 0, \quad -L < \xi^1 < L \tag{13}$$

$$T^1(\pm L, \xi^2, t) = T^2(\pm L, \xi^2, t) = 0, \quad -H < \xi^2 < H \tag{14}$$

This set of conditions represents the loading of the pre-crack by a tensile wave with a stress amplitude of 424 MPa $[(\rho c_L)_{composite}\ V_0]$ and a linear ramp from zero to that value in 0.01 μs.

TABLE 2—*Constitutive parameters for cohesive surfaces.*

Cohesive Surface Pair	σ_{max}, GPa	τ_{max}, GPa	δ_n, δ_t, nm	ϕ_0, J/m^2
Al_2O_3	34.0	78.2	0.5	46.2
TiB_2	50.0	11.5	1.0	135.9
Homogenized Al_2O_3/Ti_2B Composite	41.5	95.5	0.3	33.8
Al_2O_3/TiB_2 Interface	11.3	26.1	0.5	15.4

Finite Element Method

Finite element discretization is based on linear-displacement triangular elements arranged in a "crossed-triangle" quadrilateral pattern. Neighboring elements are connected through cohesive surfaces. Hence, for the uniform mesh region in front of the crack tip in Fig. 3, the cohesive surfaces are initially oriented along four directions, horizontal (0°), vertical (90°), positive and negative 45° (±45°). Since a very fine mesh is used (the element size is 1 μm), arbitrary fracture paths or patterns can be resolved. When the finite element discretization of the displacement field is substituted into the principle of virtual work (Eq 1), the discretized equations of motion take the form

$$\boldsymbol{M}\frac{\partial^2 \boldsymbol{U}}{\partial t^2} = \boldsymbol{R} \tag{15}$$

where $\boldsymbol{U}$ is the vector of nodal displacements, $\boldsymbol{M}$ is the nodal mass matrix, and $\boldsymbol{R}$ is the nodal force vector consisting of contributions from the bulk elements and the cohesive surfaces. A lumped mass matrix is used in Eq 15 instead of the consistent mass matrix for reasons of efficiency and accuracy during explicit time-integration Krieg and Key [*36*]. The explicit time-integration scheme based on the Newmark β-method with $\beta = 0$ and $\gamma = 0.5$ Belytschko et al. [*37*] is employed to integrate Eq 15.

Results

To illustrate the progression of fracture in the four microstructures, the distributions of σ_{22} at several different times for four calculations using these microstructures are shown on the corresponding deformed configurations in Figs. 5–8, respectively. The microstructural phase boundaries are outlined by solid dark lines for visualization of the phase morphologies. In order to quantify the progress of crack propagation, the new crack surface areas (or crack lengths in two dimensions) generated in the two phases and along matrix/reinforcement interfaces are calculated separately and analyzed. The crack length histories for these cases are shown in Figs. 9*a–d*, respectively. The crack lengths in the matrix and along the interfaces as well as the total crack length $\ell(t)$ in the composite are shown. Note that $\ell(0) = 0$, therefore, crack lengths referred to here concern new crack surfaces generated and are independent of the initial pre-crack. Since crack propagation occurs mainly in the matrix and along the phase interfaces, the crack length in the TiB_2 reinforcements is relatively small and therefore not shown. The total crack length histories $\ell(t)$ shown in Fig. 9 are differentiated with respect to time to yield the rate at which new crack surfaces are generated. Note that ℓ is the arc length along crack paths. The time derivative $d\ell/dt$ may not always represent crack speed due to possible occurrences of multiple crack fronts or simultaneous microcrack formation. However, it can be used as a relative measure of the extent of damage in the materials. On the other hand, when fracture occurs in the form of a single crack, $d\ell/dt$ represents the local crack speed as a function of time. For comparison purposes, the apparent crack speed, da/dt, where a is the projection of ℓ in the ξ^1 (horizontal) direction, is also calculated. The apparent crack length a is taken to be nondecreasing, therefore, $da/dt \geq 0$. The apparent crack speed is what is most often measured in experiments. The profiles of both $d\ell/dt$ and da/dt for the four cases are shown in Fig. 10. The oscillations in these profiles show the dynamic and unsteady nature of crack growth in the inhomogeneous material microstructure, although some of the noise may be attributed to errors in the numerical differentiation of $\ell(t)$ and $a(t)$.

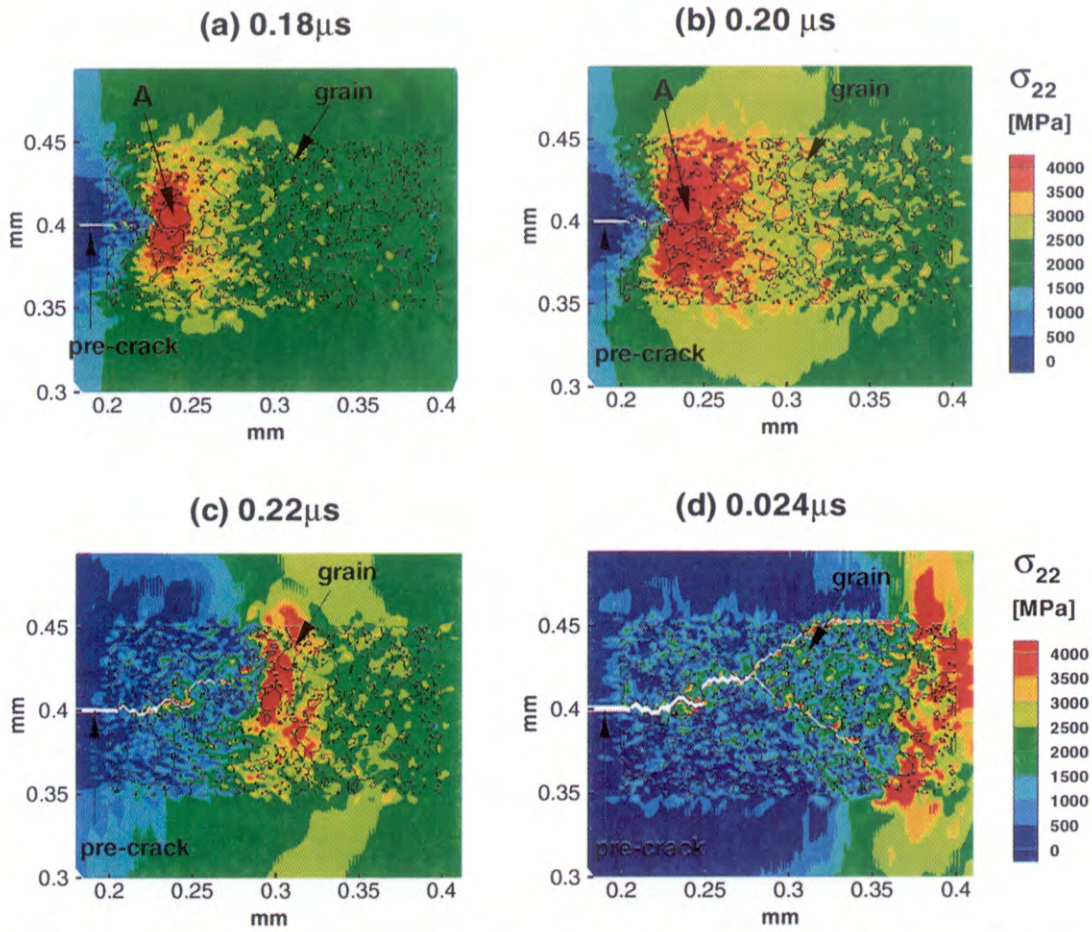

FIG. 5—*Distributions of* σ_{22} *at four different times for a specimen with microstructure in Fig. 4*a, $V_0 = 10$ *m/s.*

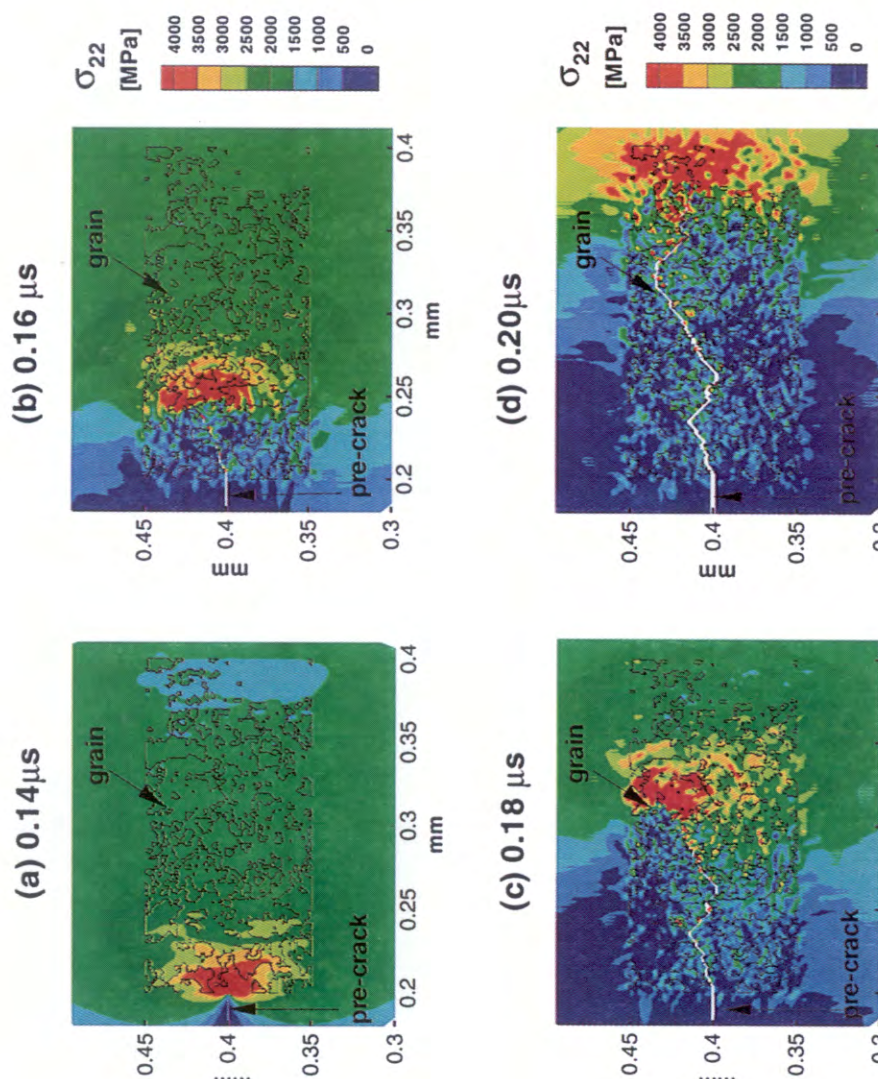

FIG. 6—*Distributions of* σ_{22} *at four different times for specimen with microstructure in Fig.* 4b, $V_0 = 10$ *m/s.*

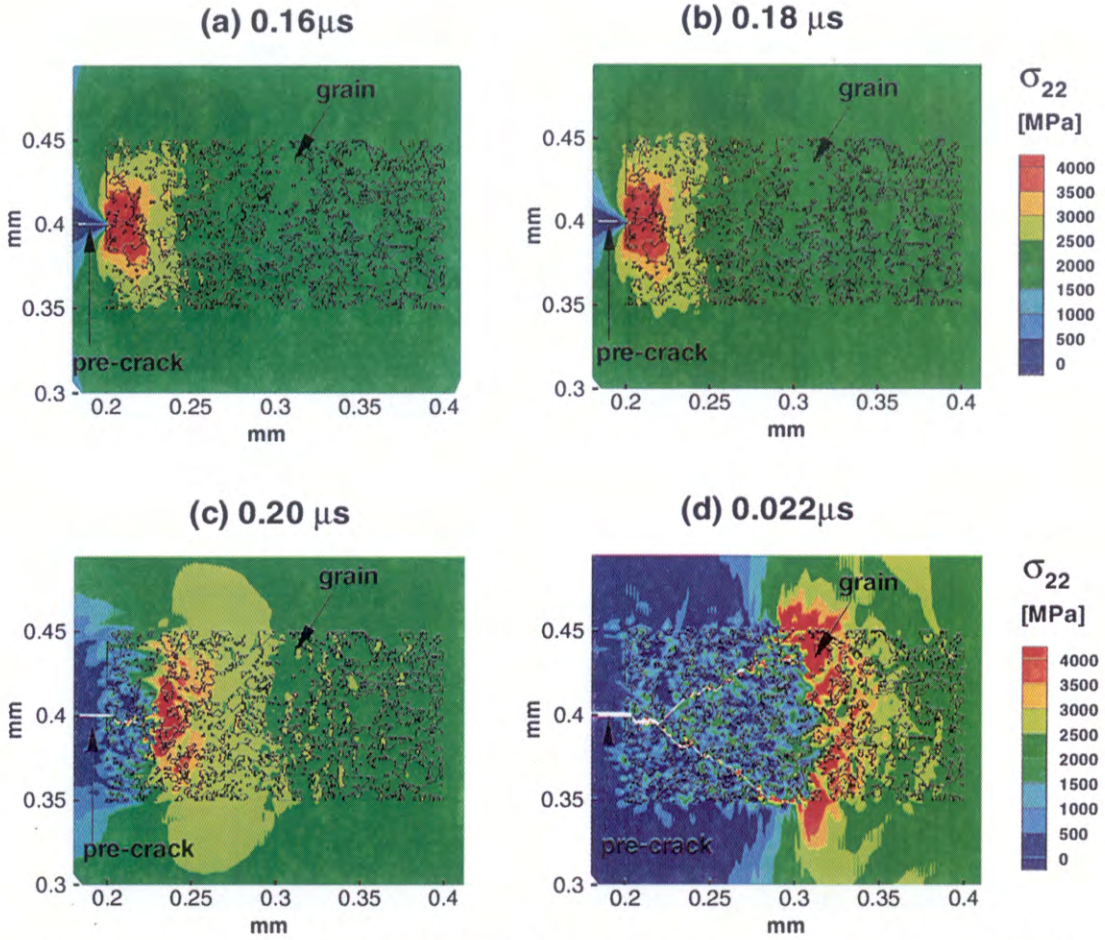

FIG. 7—*Distributions of* σ_{22} *at four different times for a specimen with microstructure in Fig. 4c,* $V_0 = 10$ *m/s.*

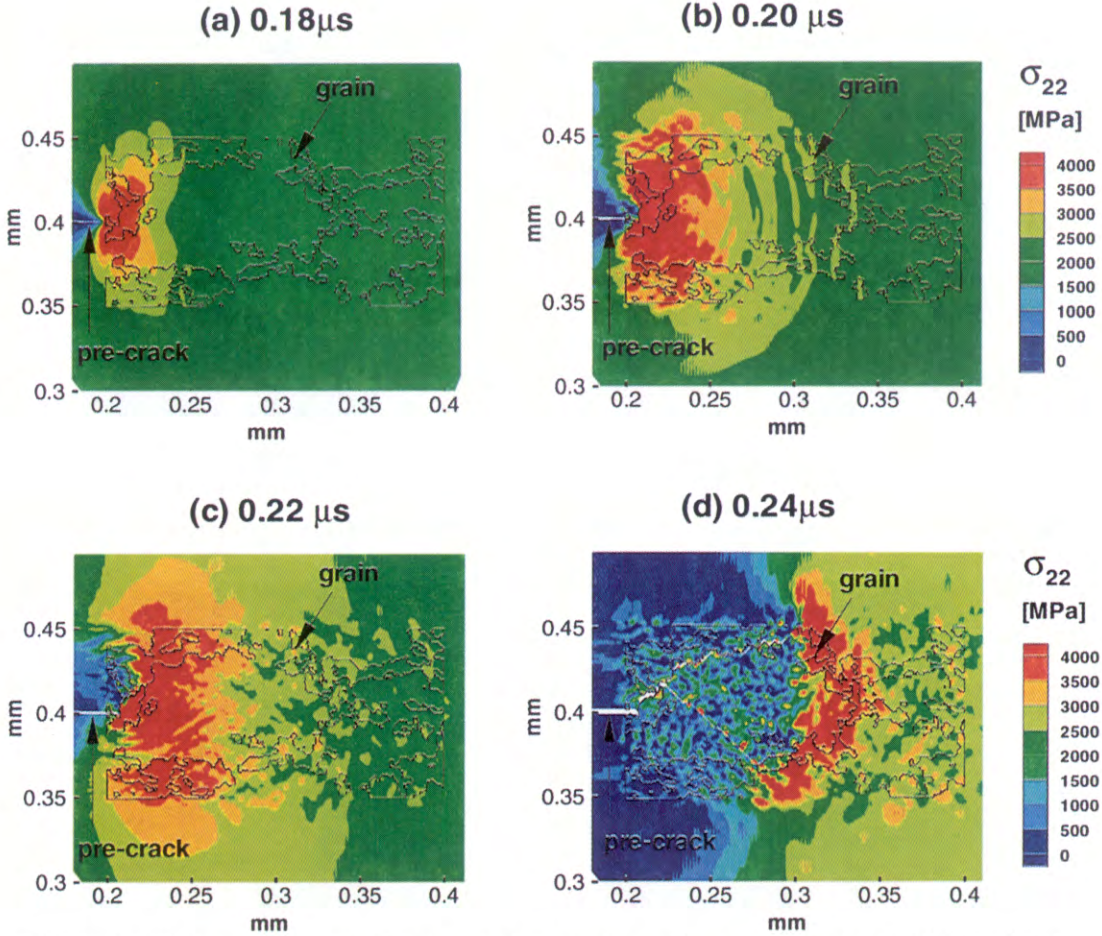

FIG. 8—*Distributions of* σ_{22} *at four different times for a specimen with microstructure in Fig.* 4d, $V_0 = 10$ *m/s.*

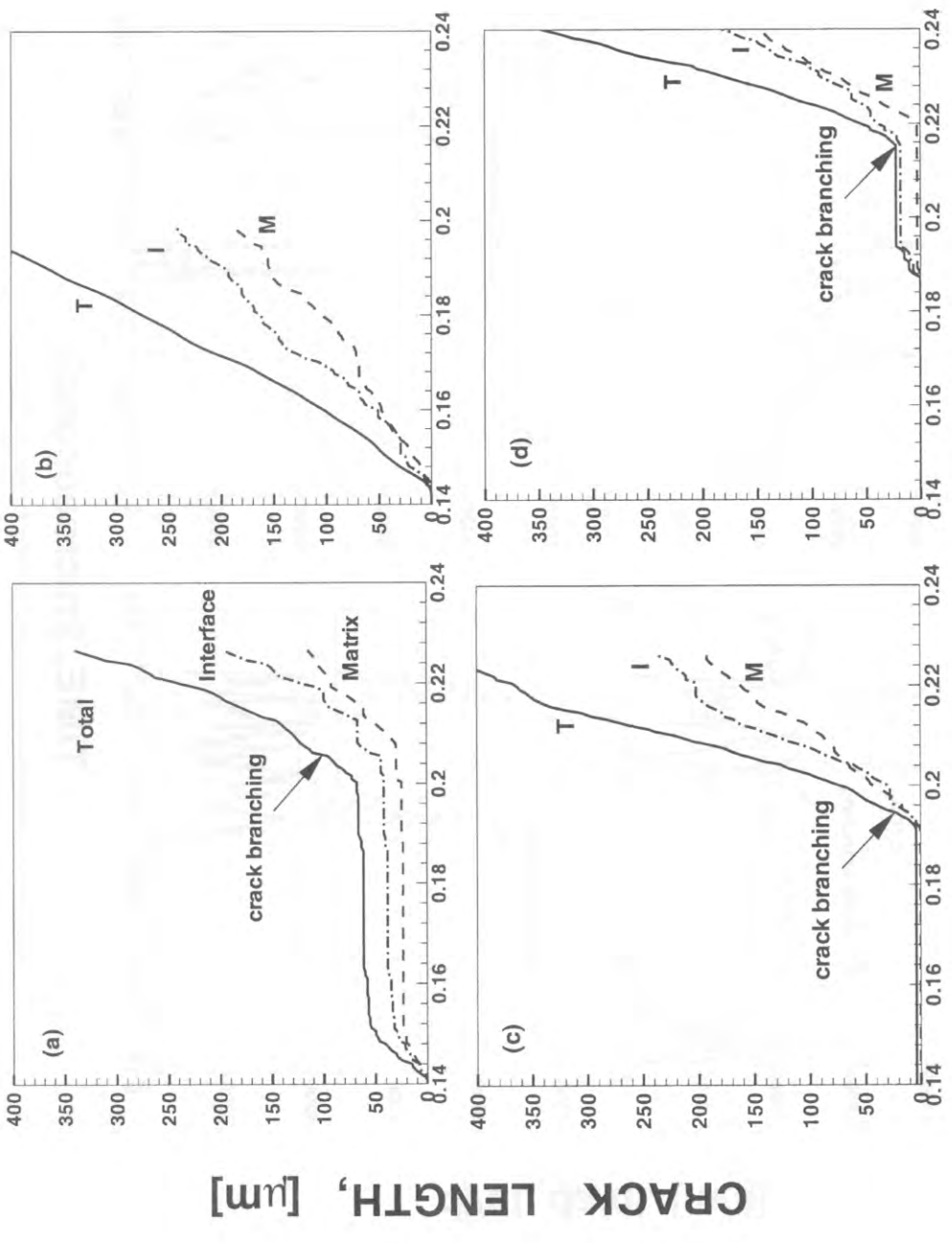
(a)
Total
Interface
Matrix
crack branching
(b)
T
I
M
(c)
T
I
M
crack branching
(d)
T
I
M
crack branching
CRACK LENGTH, [μm]
TIME, [microsecond]

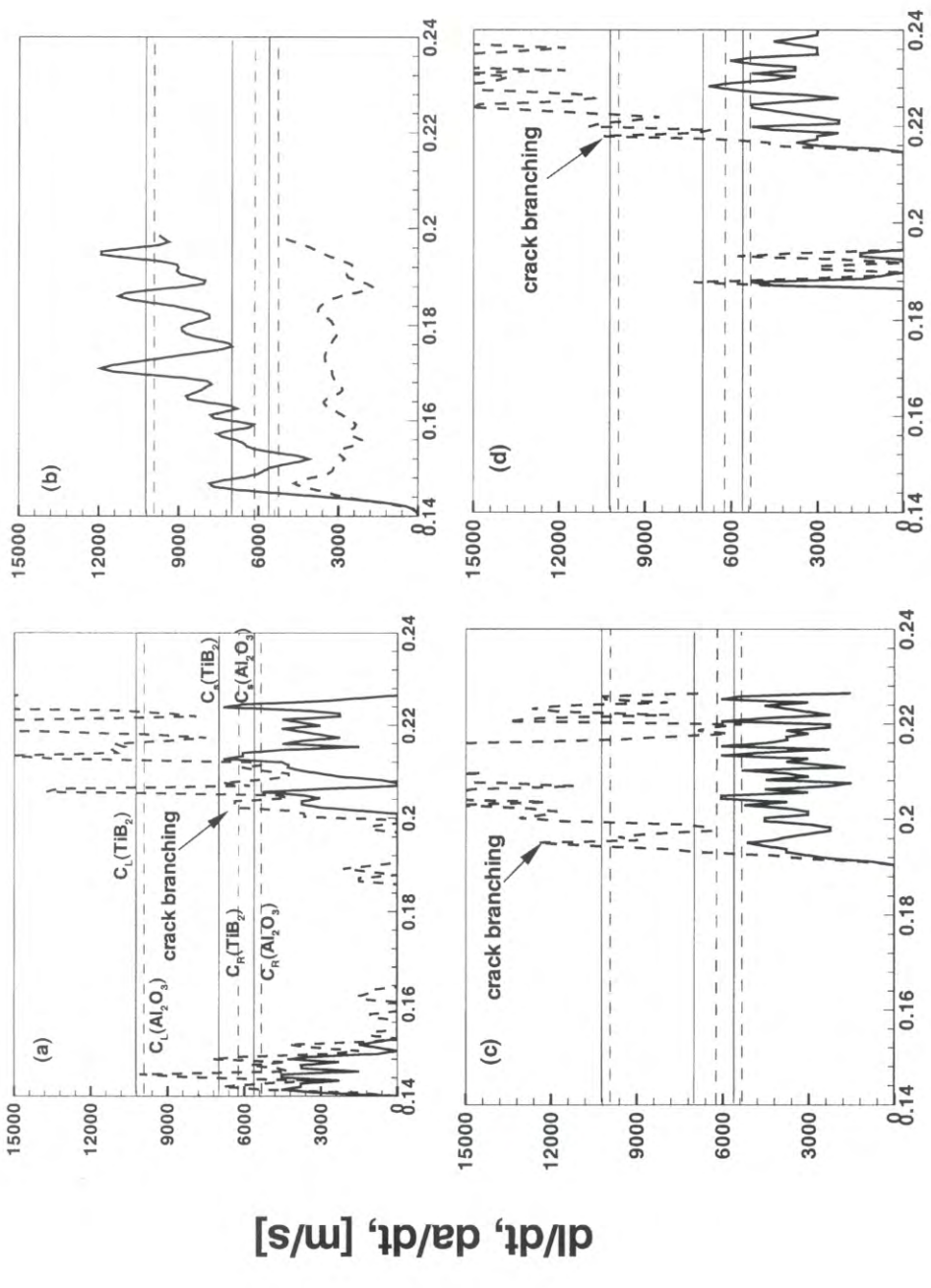

FIG. 10—*A comparison of crack speed histories for the four microstructures.*

Crack Propagation in a Heterogeneous Al_2O_3/TiB_2 Microstructure

First, the results for the microstructure in Fig. 4*a* are discussed. Figure 5 and Fig. 9*a* show that crack initiation occurs at approximately 0.14 μs. The crack first zigzags in the matrix between small TiB_2 particles and then arrests when the crack tip impinges on a large grain at point A, Figs. 5*a–b*. This grain represents a stronger obstacle to crack growth due to its higher bulk and cohesive strengths. As a result, the crack is essentially stationary between 0.15 and 0.20 μs, see Figs. 9*a* and 10*a*. There is an increase in stress intensity in front of the crack tip during this period as indicated by the size of the area with high stresses. The attainment of higher stresses allows the crack to circumvent the impeding grain through the separation of grain/matrix interface, Fig. 5*c–d*. Part of the debonding process involves primarily local tangential (shear) displacement along the interface. After the grain at A, subsequent propagation is primarily through the matrix and interfaces between small particles and the matrix. The crack eventually branches into two propagating tips at approximately 0.204 μs and their overall characteristics are the same as those for the parent crack, Fig. 5*d*. It can be seen in Fig. 9*a* that more crack surfaces are created along the phase boundaries than in the matrix, reflecting the effect of the weaker bonding between the phases compares with the cohesive strengths of the constituents.

In Fig. 10*a*, the average apparent crack speed is approximately 3300 m/s or 61% of the Rayleigh wave speed for the matrix which is the more compliant material in the two constituents in the composite. The local crack speed, on the other hand, is higher. Before crack branching at approximately 0.204 μs, the propagation of a single crack is observed (Fig. 5*a–b*) and $d\ell/dt$ represents the local crack tip speed. The average value of this local speed is approximately 6000 m/s. The plot shows that this speed approaches transonic levels, that is, above the Rayleigh wave and shear wave speeds of the matrix phase. Note that after branching two crack fronts are involved and the local crack tip speed for each is one half of what is seen in the profile. Therefore, the mean local crack tip speed is approximately 5500 m/s for each branch, well below the longitudinal wave speeds for the constituents (9939 and 10 694 m/s, respectively) and slightly lower than the mean local tip speed for the crack before branching. These results are consistent with the findings reported in Xu and Needleman [*38*,*39*] and the experimental measurements reported in Lambros et al. [*40*], Huang et al. [*41*] and Rosakis et al. [*42*] concerning crack propagation along bimaterial interfaces. Experimentally, apparent crack speeds in the intersonic range have been measured in carbon fiber/polymer matrix composites under impact loading, Rosakis et al. [*43*].

Effects of Different Microstructural Morphologies

The results in Figs. 5–8 show that crack path is significantly influenced by the microstructural phase morphologies. Fracture occurs primarily along phase boundaries and inside the matrix. Continuous and favorably oriented interfaces (parallel to the direction of crack propagation) facilitate crack growth, see Fig. 8*d*. Crack branching occurs at different times and different distances of crack extension from the initial crack tip. Also note that no branching is seen in Fig. 6 for microstructure (*b*). Two other calculations are carried out under the same loading conditions using uniform matrix or grain material properties for the microstructural region in front of the crack tip. The results show that in both cases crack branching occurs after very short distances of crack propagation in the ξ^1 direction from the pre-crack tip. Both distances are smaller than those observed in the composites here. These results demonstrate that material heterogeneities retard or prevent crack branching in composite microstructures. This observation is consistent with the same finding in Xu et al. [*31*] for

materials with inhomogeneous cohesive strengths but otherwise homogeneous bulk properties.

The time histories of the local crack speed $d\ell/dt$ and apparent crack speed da/dt for all four cases shown in Fig. 10 indicate a range of crack initiation times for the microstructures, from 0.12 to 0.19 μs. The microstructures have a clear impact on the fracture initiation time. Temporary arrest of crack propagation due to impediments of larger particles is also observed, see Fig. 9*a,d* and Fig. 10*a,d*. The apparent crack speed seems to oscillate around a mean value of approximately 3300 m/s or 61% of the Rayleigh wave speed for the matrix material in all microstructures. This average seems to be independent of the differences in the microstructural morphologies and phase sizes considered. In contrast, the local crack speed seems to be more significantly affected by the microstructural phase distributions. In Fig. 6 for microstructure (*b*), no branching occurs and the local speed reaches well into the intersonic range, that is the mean crack speed is well above the shear wave speeds of the constituents and approaches 9000 m/s or approximately 90% of the longitudinal wave speed of the matrix material, see Fig. 10*b*. Recall that this local speed represents the rate of change of arc length along crack paths and is not subject to the limit of physical wave speeds such as c_L and c_s of the bulk constituents. In Figs. 5, 7, and 8, crack branching occurs and the mean local crack speed for each tip Figs. 10*a*, *c*, and *d* is approximately 6000, 5800 and 7000 m/s for microstructures (*a*), (*c*), and (*d*), respectively. These values are lower than that in Fig. 10*b*. It appears that branching reduces local crack tip speeds while allowing overall rate of surface generation to increase.

Energy Release Rate

The evolutions of the kinetic energy $\mathcal{K}$, strain energy $\mathcal{W}$, and cohesive surface energy Φ in the whole specimen for the four cases are shown in Fig. 11. The times of crack initiation are clearly signified by upturns in the curves for Φ in (*a*), (*c*), and (*d*). In Fig. 11*c*, the crack arrests shortly after initiation. Earlier crack initiation allows more crack surfaces to be generated, resulting in more energy to be expended in the process (higher Φ) and less strain energy to be stored in the specimen (lower $\mathcal{W}$). This is the case in Figs. 11*a–c* in which the crack initiation times are between 0.124 and 0.144 μs. On the other hand, delayed crack initiation (Figs. 11*d*, approximately 0.192 μs) corresponds to less new crack surfaces and less energy consumption (lower Φ), leading to more strain energy stored in the specimen (higher $\mathcal{W}$). Although crack branching has a clear signature in the profiles for Φ and $\mathcal{K}$ in Fig. 11*a* for microstructure (*a*), such an effect can not be easily identified in Figs. 11*b–d* for other microstructures.

To analyze the energy expended during fracture, the total crack surface energy Φ_{crack} is calculated for each case. This energy is

$$\Phi_{\text{crack}} = \int_{S_{\text{crack}}} \phi_0(x) dS \tag{16}$$

where S_{crack} is defined as the part of the internal surface S_{int} that satisfies $\phi(\Delta) \geq 0.99\phi_0$. In the current analysis, Φ_{crack} is calculated for the first 350 μm of the total crack length $\ell(t)$, or for $0 \leq \ell(t) \leq 350$ μm. Note that it takes different amounts of time to reach this crack length in different microstructures. The calculated values of Φ_{crack}, the apparent crack length a, and the time t at a total crack length of $\ell = 350$ μm for the four microstructures are listed in Table 3. Figure 12 compares the histories of Φ_{crack} as function of ℓ and the apparent crack length a for the four cases considered. This figure and the table show that there is a significant

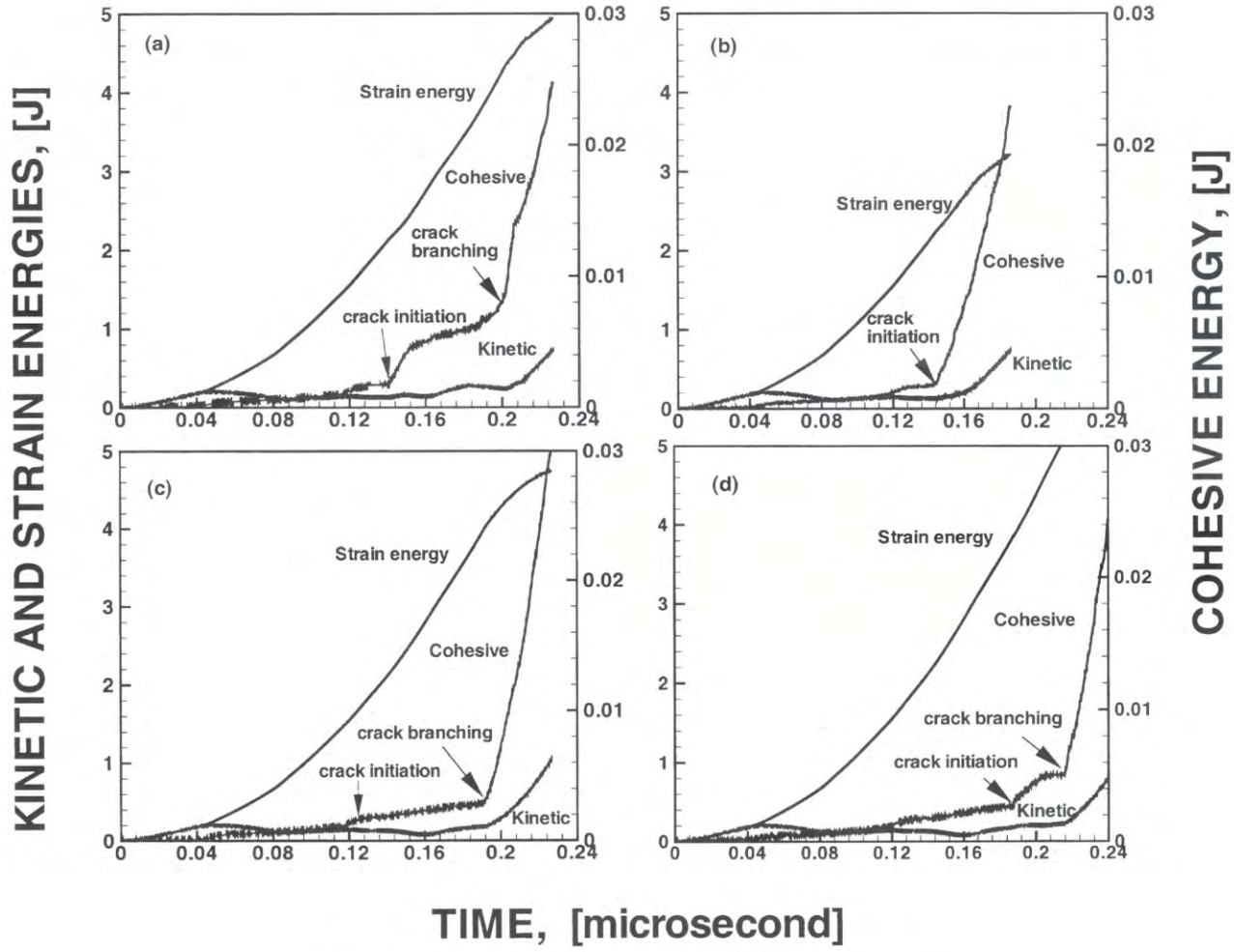

FIG. 11—*A comparison of energy evolutions for the four microstructures.*

TABLE 3—*Average energy release rates for different microstructures.*

Microstructure	Average size of TiB_2, μm	ϕ_{crack}, $\times 10^{-3}$ J	Time, μs	$a(t)$ at $\ell = 350$ μm	$\frac{\partial \Phi_{crack}}{\partial \ell}$, J/m	$\frac{\partial \Phi_{crack}}{\partial a}$, J/m
(*a*)	10–20	12.5	0.23	122	35.7	102.5
(*b*)	8–10	11.0	0.19	142	31.4	77.5
(*c*)	1–2	10.3	0.22	102	28.6	98.0
(*d*)	20 × 100	12.1	0.24	110	34.3	110.0

variation of fracture energy among the four microstructures. The waviness in the curves reflects the different values of work of separation ϕ_0 in different constituents and along matrix/reinforcement interfaces. The energy release rate or energy consumption per unit length of crack generated is

$$\mathcal{G} = \frac{\partial \Phi_{crack}}{\partial \ell} \tag{17}$$

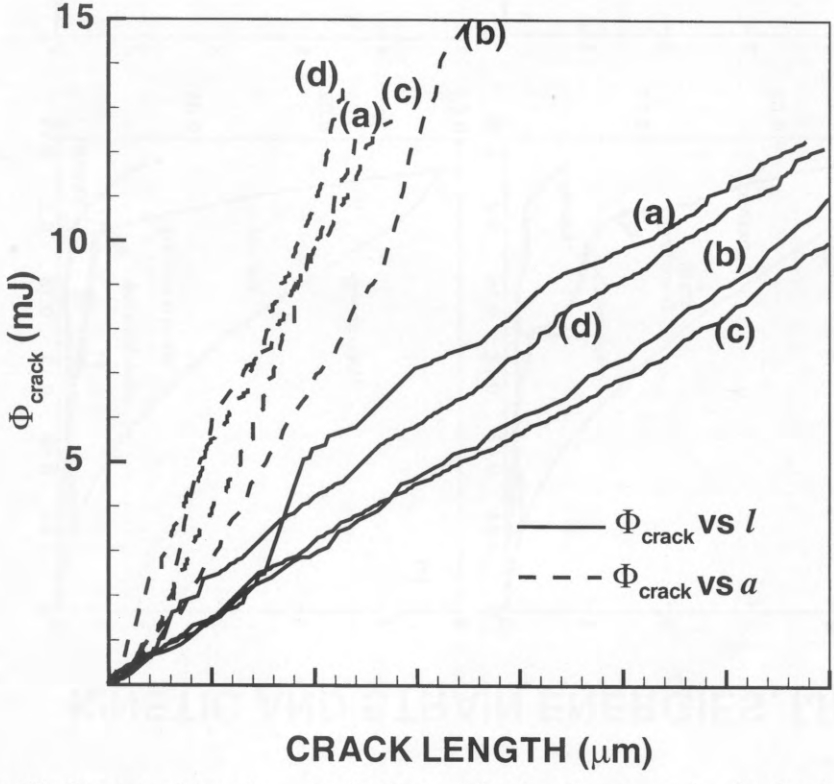

FIG. 12—*Fracture energy Φ_{crack} as functions of local and apparent lengths for the four microstructures.*

When fracture occurs in the form of a single crack propagating solely in the horizontal direction, $\ell = a$, $\mathcal{G} = \partial\Phi_{crack}/\partial\ell = \partial\Phi_{crack}/\partial a$ represents the energy release rate for crack propagation in the regular fracture mechanics sense. Figure 13 compares histories of the instantaneous energy release rate defined in Eq 17 as a function of ℓ for the four cases analyzed. In these profiles, there are three characteristic levels which correspond to the works of separation inside the grains ($\phi_0 = 135.9$ J/m^2), inside the matrix ($\phi_0 = 46.2$ J/m^2) and along the matrix/reinforcement interfaces ($\phi_0 = 15.4$ J/m^2). Instantaneous $\mathcal{G}$ values between the above three levels occur when simultaneous fracture happens at multiple sites with different values of ϕ_0. The profiles in the plot show that such incidents occur quite frequently for all four microstructures. Most of these are microcrack sites along the main crack path or paths seen in Figs. 5–8, since all four cases show only one main crack (Fig. 6) or one crack followed by two branches and no large scale microcracking is observed. It can be seen that $\mathcal{G}$ oscillates mainly between 46.2 J/m^2 and 15.4 J/m^2, providing a quantitative measure for the observation made from Figs. 5–9 that crack propagation is primarily through the matrix and the phase boundaries. To facilitate comparison, the average values of $\partial\Phi_{crack}/\partial\ell$ and $\partial\Phi_{crack}/\partial a$ corresponding to the four profiles in Fig. 13 are listed in Table 3. Note that it takes different amounts of time for ℓ to reach 350 μm in different microstructures. For higher resistance to fracture, it is desirable to induce cracks to go through the hard TiB_2 reinforcements, as seen in Fig. 5*a* and indicated by the spikes of $\mathcal{G}$ values up to 135.9 J/m^2 in Fig. 13*a*. It can be seen that as the average size of TiB_2 reinforcements is decreased from microstructures (*a*) to (*c*) the average energy release rate $\partial\Phi_{crack}/\partial\ell$ decreases, reflecting decreasing amounts of crack growth in higher strength TiB_2 or matrix in Figs. 13*b* and 13*c*. Indeed, Fig. 13*c* shows that no fracture occurs inside TiB_2 in microstructure (*c*) for the duration analyzed. Also, there seems to be a higher fraction of fracture along matrix/grain interfaces that has the lowest work of separation among the three types of fracture sites. The larger sizes of the TiB_2 reinforcements in microstructure (*d*) cause its average value of $\partial\Phi_{crack}/\partial\ell$ to be higher. Clearly, there is significant fracture inside the TiB_2 phase, as indicated in Fig. 13*d*. However, the existence of continuous and favorably oriented TiB_2/Al_2O_3 boundaries inherent in the morphology of a network of TiB_2 filled with Al_2O_3 colonies also allow cracks to propagate along the interfaces with relatively low hindrance.

Discussions

The results discussed above show that it is possible to change the fracture resistance of brittle composites by altering microstructural morphologies through favorable material processing conditions. It is conceivable that energy release rates higher than those calculated here may be achieved by other microstructural morphologies not considered since the four variations analyzed represent only a small sample of microstructural morphologies that can be produced by various methods of material synthesis. This analysis did not consider the effects of varying the bulk properties for each phase on the failure behavior of the composites. There are ample opportunities for performance enhancement through the use of constituents with dissipation mechanisms. The effects of various elasto-plastic constituents on fracture should be characterized in future analyses. Interfacial bonding strength between the phases is another factor that can significantly influence the behavior of the materials. In a related analysis, it is found that under certain loading rates this interphase bonding plays a role in determining the characteristics of fracture or the mode of fracture in the TiB_2/Al_2O_3 composites, Zhai et al. [*35*]. Specifically, when weak interfacial strength exists, microcrack initiation and growth are the principal mode of failure; whereas when strong interfacial strength is derived from material processing, the advancement of a dominant crack and crack branching are observed. It is expected that the fracture behavior of heterogeneous materials

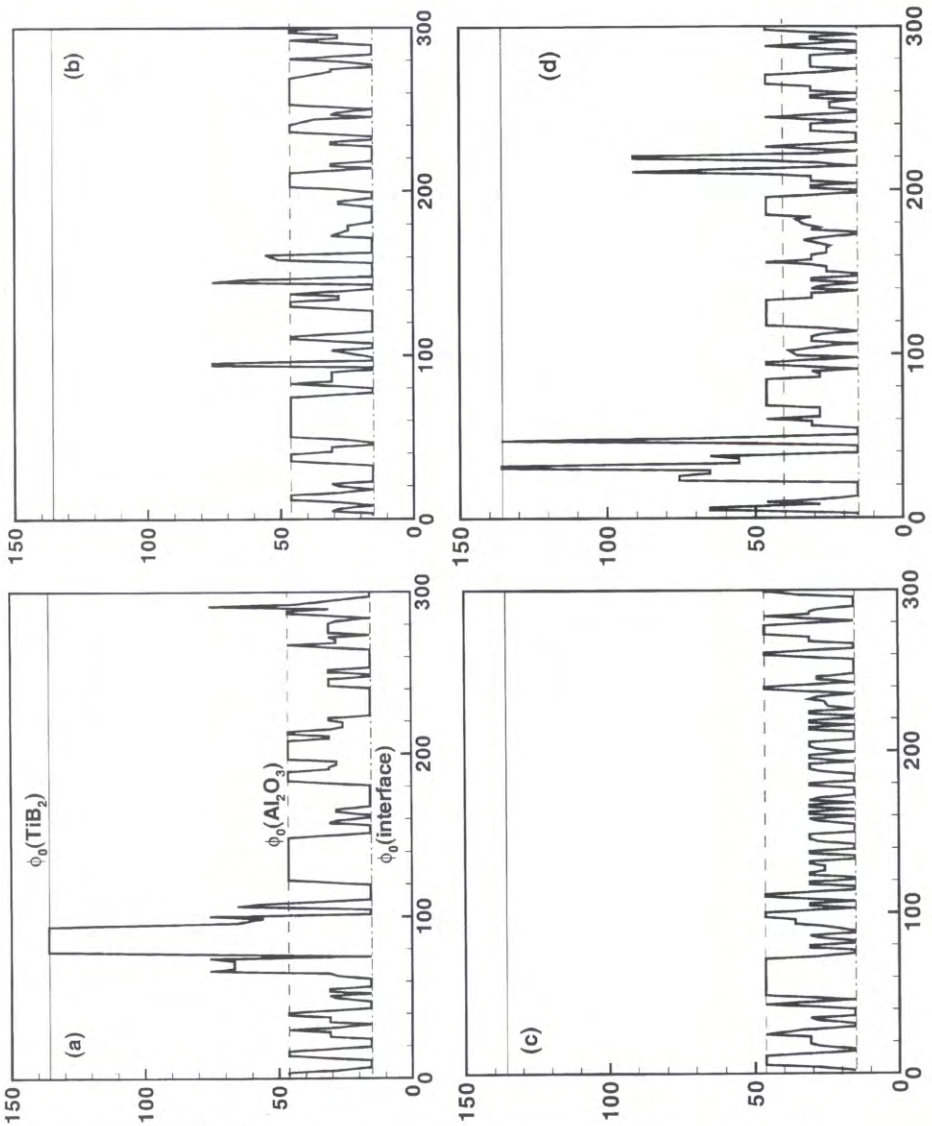

FIG. 13—*Energy release rate as functions of local and apparent crack lengths for the four microstructures.*

is also loading rate sensitive due to the rate-dependence of bulk constituent behavior and inertia. These issues shall be addressed in future publications.

A micromechanical model that provides explicit account for arbitrary microstructures and arbitrary is used here. The approach incorporates both a constitutive law for the bulk solid constituents and a constitutive law for fracture surfaces. The interfacial separation law can be regarded as a phenomenological characterization of atomic interaction forces. This approach is especially appropriate for analyzing microscopic fracture over a range of length scales because (i) material separation is a natural outcome of bulk constitutive response, interfacial behavior, microstructure, and loading; and (ii) the formulation is free from any fracture initiation, growth, and coalescence criteria that are necessary in most other continuum analyses, therefore circumventing the limitations of failure criteria that are valid only over certain length scales, such as continuum criteria based on the existence of K-fields. This framework allows for a unified treatment of mix-mode fracture without resorting to the differentiation of fracture into separate modes. The elimination of the need for ad hoc criteria is accompanied by the introduction of the need for interfacial separation laws at various microscopic settings of interest. Therefore, an important task is the development of interfacial constitutive laws appropriate for specific materials and length scales. For specific forms of cohesive laws, the determination of cohesive parameters for constituents is another relevant issue. For example, over a certain size scale the calibration of model parameters by assuming $\phi_0 = (1 - v^2)K_{IC}^2/E$ may be justifiable for brittle constituents. However, the same assumption may become indefensible if the objective is to quantify nano-scale fracture mechanisms. Indeed, there is a serious lack of experimental characterization as well as understanding for interfacial constitutive behaviors on the sub-micron length scales. Issues include, among others, dissipation in the separation process and the gradient-dependence of traction along interfaces. Kim [*44*] proposed a relation for interface decohesion that accounts for nonlocal effects on the nano-scale. Significant challenges and opportunities exist for experimental and analytical research on nano-scale and micro-scale interfacial separation mechanisms. As such separation laws are made available and as long as appropriate bulk response laws are used including the quasi-continuum formulation of Tadmor et al. [*45*], the unique framework off analysis employed here represents a systematic and consistent approach for explicit modeling of fracture over a wide range off length scales.

Conclusions

The dynamic failure behavior in a class of Al_2O_3/TiB_2 composites is analyzed in the context of fracture in a centered-cracked specimen under remote tensile loading. Numerical simulations are carried out under the conditions of plane strain. A micromechanical framework of analysis has been developed and used, providing an explicit account for arbitrary material microstructural morphologies and resolution for arbitrary, unconstrained fracture patterns. The approach combines constitutive description of bulk material responses and characterization of fracture surface cohesion. The framework of analysis allows mixed-mode fracture behavior of materials with composite microstructures to be examined without resorting to any mode-dependent fracture initiation or propagation criteria. In this analysis, both the bulk and the interfacial constitutive laws are assumed to be hyperelastic. The results of numerical simulations demonstrated the microscopic phase distribution and phase size scale can significantly influence the fracture behavior. Due to their higher cohesive strength and therefore higher energy release rate, TiB_2 reinforcements represent stronger obstacles to the growth of cracks and increase the energy required in generating the same amount of crack surfaces. The increase in fracture resistance is higher in microstructures with larger

TiB_2 particles. A 25% variation in average energy release rate is observed for the four microstructures of actual Al_2O_3/TiB_2 composites prepared by high-temperature synthesis.

Acknowledgment

Support from the Army Research Office through grant DAAG55-98-1-0454 is gratefully acknowledged. Calculations reported are carried out on the Cray Computers at the San Diego Supercomputer Center, Jet Propulsion Laboratory and the Goddard Space Center. M. Zhou would like to thank A. Needleman and X.-P. Xu for helpful discussions. Thanks are extended to K. V. Logan for providing micrographs of Al_2O_3/TiB_2 composites used in this research.

References

[1] Shockey, D. A., Curran, D. R., Seaman, L., Rosenberg, J. T., and Peterson, S. F., "Fragmentation of Rock Under Dynamic Loads," *International Journal of Rock Mechanics,* Vol. 11, 1974, pp. 303–317.

[2] Grady, D. E. and Kipp, M. E., "The Micromechanics of Impact Fracture of Rock," *International Journal of Rock Mechanics,* Vol. 16, 1979, pp. 293–302.

[3] Lankford, J., "Dynamic Compressive Fracture in Fiber-reinforced Ceramic Matrix Composites," *Material Science and Engineering A: Structural Materials: Properties, Microstructure and Processing,* Vol. A107, 1989, pp. 261–268.

[4] Shockey, D. A., Seaman, L., and Curran, D. R., "The Micro-Statistical Fracture Mechanics Approach to Dynamic Fracture Problems," *International Journal of Fracture,* Vol. 27, 1985, pp. 145–157.

[5] Brockenbrough, J. R., Suresh, S., and Duffy, J., "An Analysis of Dynamic Fracture in Microcracking Solids," *Philosophy Magazine A,* Vol. 58, 1988, pp. 619–634.

[6] Longy, F. and Cagnoux, J., "Plasticity and Microcracking in Shock-loaded Alumina," *Journal of American Ceramic Society,* Vol. 72, 1989, pp. 971–979.

[7] Kishi, T., Takeda, N., and Kim, B. N., "Dynamic Fracture Toughness and Microstructural Fracture Mechanisms in Ceramics," *Ceramic Engineering and Science Process,* Vol. 11, No. 7–8, 1990, pp. 650–664.

[8] Curtin, W., "Theory of Mechanical Properties of Ceramic-Matrix Composites," *Journal of American Ceramic Society,* Vol. 74, 1991, pp. 2837–2845.

[9] Shockey, D. A., Machand, A. H., Skaggs, S. R., Cort, G. E., Burkett, M. W., and Parker, R., "Failure Phenomenology of Confined Ceramic Targets and Impact Rods," *International Journal of Impact Engineering,* Vol. 9, 1990, pp. 263–275.

[10] Suresh, S., Nakamura, T., Yeshurun, Y., Yang, K. H., and Duffy, J., "Tensile Fracture Toughness of Ceramic Materials: Effects of Dynamic Loading and Elevated Temperatures," *Journal of American Ceramic Society,* Vol. 73, 1990, pp. 2457–2466.

[11] Yang, K. -H. and Kobayashi, A. S., "Dynamic Fracture Response of Alumina and Two Ceramic Composites," *Journal of American Ceramic Society,* Vol. 73 No. 8, 1990, pp. 2309–2315.

[12] Evans, A. G., "The Mechanical Properties of Reinforced Ceramic, Metal and Intermetallic Matrix Composites," *Material Science and Engineering,* Vol. A143, 1991, pp. 63–76.

[13] Kishi, T., "Dynamic Fracture Toughness in Ceramic and Ceramics Matrix Composites," *Engineering Fracture Mechanics,* Vol. 40, 1991, pp. 785–790.

[14] Kobayashi, A. S., "Dynamic Fracture of Ceramics and Ceramic Composites," *Materials Science and Engineering,* Vol. A143, 1991, pp. 111–117.

[15] Espinosa, H. D., Raiser, G., Clifton, R. J., and Ortiz, M., "Experimental Observation and Numerical Modeling of Inelasticity in Dynamic Loaded Ceramics," *Journal of Hard Materials,* Vol. 3, 1992, pp. 285–313.

[16] Ahrens, T. J. and Rubin, A. M., "Impact-Induced Tensional Failure in Rock," *Journal of Geophysics Research,* Vol. 98, 1983, pp. 1185–1203.

[17] Vekinis, G., Ashby, M. F., Shercliff, H., and Beaumont, P. W., "The Micromechanics of Fracture of Alumina and Ceramic-Based Fiber Composite: Modeling the Failure Processes," *Composites Science and Technology,* Vol. 48, 1993, pp. 325–330.

[18] Lankford, J., "Effect of Hydrostatic Pressure and Loading Rate on Compressive Failure of Fiber-Reinforced Ceramic-matrix Composites," *Compos. Sci. Tech.,* Vol. 51, 1994, pp. 537–543.

[19] Woodward, R. L., Gooch, W. A., O'Donnell, R. G., Oerciballi, W. J., Baxter, B. J., and Oattie, S. D., "A Study of Fragmentation in the Ballistic Impact of Ceramics," *International Journal of Impact Engineering,* Vol. 15, 1994, pp. 605–618.

[20] Zhou, S. J. and Curtin, W. A., "Failure of Fiber Composites: A Lattice Green Function Model," *Acta Metallurgic Material,*" Vol. 43, 1995, pp. 3093–3104.

[21] Seaman, L., Curran, D. R., and Murri, W. J., "A Continuum Model for Dynamic Tensile Microstructure and Fragmentation," *Journal of Applied Mechanics,* Vol. 52, 1985, pp. 593–600.

[22] Curran, D. R., Seaman, L., and Shockey, D. A., "Dynamic Failure of Solids," *Physics, Reports,* Vol. 147, 1987, pp. 253–388.

[23] Curran, D. R., Seaman, L., Cooper, T., and Shockey, D. A., "Micromechanical Model for Continuum and Granular Flow of Brittle Materials Under High Strain Rate Application to Penetration of Ceramic Targets," *International Journal of Impact Engineering,* Vol. 13, 1993, pp. 53–58.

[24] Rajendran, A. M., "Modeling the Impact Behavior of AD85, Ceramic under Multiaxial Loading," *International Journal of Impact Engineering,* Vol. 15, 1994, pp. 749–768.

[25] Johnson, G. R. and Holmquist, T. J., "Computational Constitutive Model for Brittle Materials Subjected to Large Strains, High Rates, and High Pressure," M. A. Meyers, L. E. Murr, and K. P. Staudhammer, Editors, *Shock Wave and High Strain Rate Phenomena in Materials,* 1992, pp. 1075–1081.

[26] Walter, J., "Material Loading for Terminal Ballistic Simulation, Technical Report," U.S. Army Research Lab., MD, 1992.

[27] Espinosa, H. D. and Brar, N. S., "Dynamic Failure Mechanisms of Ceramic Bars: Experiments and Numerical Simulations," *Journal of Mechanics and Physics of Solids,* Vol. 43, 1995, pp. 1615–1638.

[28] Ravichandran, G. and Subhash, G., "A Micromechanical Model for High Strain Rate Behavior of Ceramics," *International Journal of Solids and Structures,* Vol. 32, 1995, pp. 2627–2646.

[29] Gao, H. J. and Klein, P., "Numerical Simulation of Crack Growth in an Isotropic Solid with Randomized Cohesive Bonds," *Journal of Mechanics and Physics of Solids,* Vol. 46, 1998, pp. 187–218.

[30] Xu, X. -P. and Needleman, A., "Numerical Simulations of Fast Crack Growth in Brittle Solids," *Journal of Mechanics and Physics of Solids,* Vol. 42, 1994, pp. 1397–1434.

[31] Xu, X. -P., Needleman, A., and Abraham, F. F., "Effect of Inhomogeneities of Dynamic Crack Growth in an Elastic Solid," *Modeling & Simulation Materials Science and Engineering,* Vol. 5, 1997, pp. 489–516.

[32] Camacho, G. T. and Ortiz, M., "Computational Modeling of Impact Damage in Brittle Materials," *International Journal of Solids and Structures,* Vol. 33, No. 20–22, 1996, pp. 2899–2983.

[33] Ortiz, M., "Computational Micromechanics," *Computational Mechanics,* Vol. 18, 1996, pp. 321–338.

[34] Logan, K. V., "Composite Ceramics, Final Technical Report," USSTACOM DAAEO7-95-C-R040, 1996.

[35] Zhai, J. and Zhou, M., "Finite Element Analysis of Micromechanical Failure Modes in Heterogeneous Brittle Solids," *International Journal of Fracture,* special issue on failure modes in solids, 1998.

[36] Krieg, R. D. and Key, S. W., "Transient Shell Response by Numerical Time Integration," *International Journal of Numerical Method in Engineering,* Vol. 7, 1973, pp. 273–286.

[37] Belytschko, T., Chiapetta, R. L., and Bartel, H. D., "Efficient Large Scale Non-linear Transient Analysis by Finite Elements," *International Journal of Numerical Method in Engineering,* Vol. 10, 1976, pp. 579–596.

[38] Xu, X.-P. and Needleman, A., "Numerical Simulations of Dynamic Interfacial Crack Growth Allowing for Crack Growth Away From the Bond Line," *International Journal of Fracture,* Vol. 74, 1995, pp. 253–275.

[39] Xu, X. -P. and Needleman, A., "Numerical Simulations of Dynamic Crack Growth Along an Interface," *International Journal of Fracture,* Vol. 74, 1996, pp. 289–324.

[40] Lambros, J. and Rosakis, A. J., "Shear Dominated Transonic Interfacial Crack Growth in a Bimaterial—I. Experimental Observations," *Journal of Mechanics and Physics of Solids,* Vol. 43, 1995, pp. 169–188.

[41] Huang, Y., Wang, W., Liu, C., and Rosakis, A. J., "Intersonic Interfacial Crack Growth in a Bimaterial: An Investigation of Crack Face Contact," *Journal of Mechanics and Physics of Solids,* 1998, in press.

[42] Rosakis, A. J., Samudrala, O., and Singh, R. P., and Shukla, A., "Intersonic Crack Propagation in Bimaterials," *Journal of Mechanics and Physics of Solids,* in press, 1998.

[*43*] Rosakis, A. J., Liu, C., Stout, M. G., and Lambros, J., "Dynamic Fracture of Unidirectional Composites," IMECE, Nov. 16–21, 1997, manuscript in preparation.
[*44*] Kim, K. S., "Nanomechanics of defects in crystalline solids," in preparation.
[*45*] Tadmor, E. B., Ortiz, M., and Phillips, R., "Quasicontinuum Analysis of Defects in Solids, *Philosophy Magazine,*" Vol. 73, 1996, pp. 1529–1563.